

Latent-space variational data assimilation in two-dimensional turbulence

Andrew Cleary*

Department of Mechanical Engineering, Johns Hopkins University, Baltimore, MD 21218, USA

Qi Wang

Department of Aerospace Engineering, San Diego State University, San Diego, CA 92182, USA

Tamer A. Zaki†

*Department of Mechanical Engineering, Johns Hopkins University, Baltimore, MD 21218, USA and
Department of Applied Math and Statistics, Johns Hopkins University, Baltimore, MD 21218, USA*

(Dated: February 16, 2026)

Starting from limited measurements of a turbulent flow, data assimilation (DA) attempts to estimate all the spatio-temporal scales of motion. Success is dependent on whether the system is observable from the measurements, or how much of the initial turbulent field is encoded in the available measurements. Adjoint-variational DA minimizes the discrepancy between the true and estimated measurements by optimizing the initial velocity or vorticity field (the ‘state space’). Here we propose to instead optimize in a lower-dimensional latent space which is learned by implicit rank minimizing autoencoders. Assimilating in latent space, rather than state space, redefines the observability of the measurements and identifies the physically meaningful perturbation directions which matter most for accurate prediction of the flow evolution. When observing coarse-grained measurements of two-dimensional Kolmogorov flow at moderate Reynolds numbers, the proposed latent-space DA approach estimates the full turbulent state with a relative error improvement of two orders of magnitude over the standard state-space DA approach. The small scales of the estimated turbulent field are predicted more faithfully with latent-space DA, greatly reducing erroneous small-scale velocities typically introduced by state-space DA. Furthermore, latent-space DA is demonstrated to be robust to noisy measurements at the range of Reynolds numbers considered. These findings demonstrate that the observability of the system from available data can be greatly improved when turbulent measurements are assimilated in the right space, or coordinates.

I. INTRODUCTION

Assimilating experimental data into numerical simulations improves the fidelity of the simulations and enables nonintrusive access to all the scales of the estimated flow. However, the estimation of turbulence from limited measurements is a difficult ill-posed problem [1]. Turbulence presents challenges such as the chaotic nature of the forward and dual problems, the non-uniqueness of solutions consistent with the measurements, and the introduction of erroneous small-scale velocities that decay over the solution trajectory.

Conventional data assimilation utilizes the measurements to navigate the state-space representation of turbulence, and to directly estimate the velocity or vorticity field that justifies the measurements. However, the state-space representation of turbulence is not necessarily suitable for this task. In this work, we propose to first map from the measurements to a pre-designed latent space, from which the full turbulent field can be subsequently decoded. We show that the accuracy of the estimated turbulent field can be significantly improved over a broad range of scales by interpreting the turbulent measurements in this latent space, when compared to the estimation using the state-space coordinates.

The term latent space refers to a low-dimensional and interpretable representation of the turbulent field, whether by familiar modal decompositions [2], or by non-linear autoencoder transformations [3]. Physical insights of complex dynamical systems can be gleaned from these low-dimensional latent spaces [4]. Rank-minimizing autoencoders have successfully learned parsimonious representations of chaotic systems such as the Lorenz system, the Kuramoto-Sivashinsky equation and the lambda-omega reaction-diffusion system [5]. The latent spaces of such autoencoders have yielded insights on the nature of bursting events and the dynamical relevance of unstable periodic orbits in forced two-dimensional (2D) turbulence [6].

In the context of turbulence estimation, data-driven methods have been used to directly super-resolve limited instantaneous observations to the full flow state [e.g. 7]. Another super-resolution study considered a time-history

* acleary7@jh.edu

† t.zaki@jhu.edu

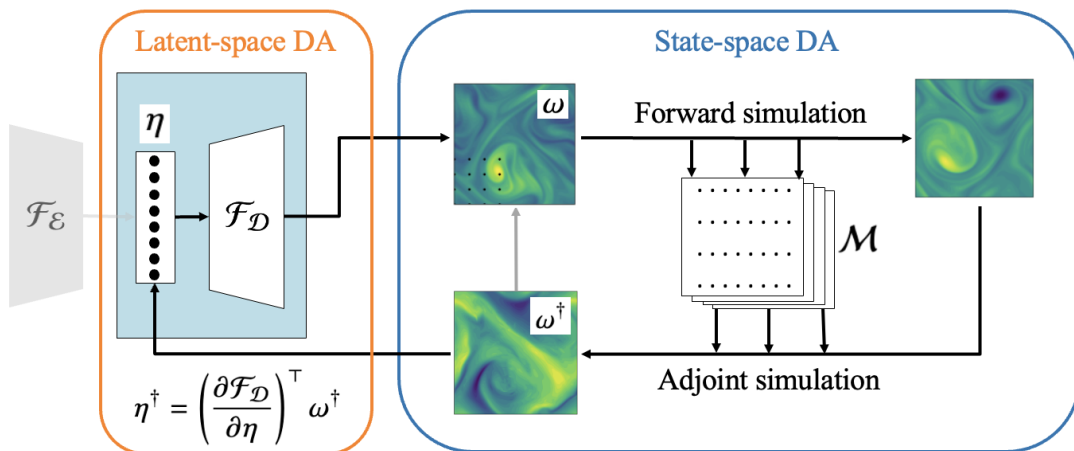


FIG. 1. Schematic of latent-space data assimilation. The latent representation η is mapped to state space ω by the decoder \mathcal{F}_D , where the adjoint field ω^\dagger is computed. The gray arrow closes the standard, state-space ‘loop’. In latent-space assimilation, the latent state is updated by the transformed adjoint field η^\dagger . Sensor resolution is indicated by the lattice of black dots in the lower left corner of ω .

of scarce measurements and inferred the pressure field of forced isotropic turbulent flow [8]. Machine-learning and classical adjoint DA methods to estimate turbulence have been pursued mostly separately, with a few exceptions including the following examples: Du *et al.* [9] compared the estimation of wall turbulence using physics-informed neural networks and adjoint-variational techniques. Page [10] modified the training of super-resolution networks to incorporate a time-forward Navier-Stokes evolution in the output, and a comparison to future data. Most recently, Weyrauch *et al.* [11] used the output of this super-resolution network as an initial guess to adjoint-variational DA. While this last effort has interfaced data-driven methods and adjoint-variational DA, the two techniques were not fully integrated.

Relatedly, some data-driven methods have been incorporated into statistical filtering approaches for data assimilation [12] and into adjoint-variational approaches to approximate the time forward operator [13], but neither of these cases exactly satisfy the governing dynamical equations. In this work, we combine a learned space that is discovered using data-driven methods with the physics constraints of adjoint-variational DA. This integration significantly enhances the observability of turbulence systems and their estimation across a wider range of scales, while still exactly satisfying the dynamical equations. In §II, we outline the flow configuration studied and summarize the standard variational DA procedure. In §III, we present the proposed latent-space DA procedure. In §IV, we compare and interpret the improved performance of latent-space DA. We conclude in §V.

II. STATE-SPACE DATA ASSIMILATION

We consider Kolmogorov flow, which is monochromatically forced 2D turbulence on a square and doubly periodic domain [14]. The out-of-plane vorticity $\omega = \partial_x v - \partial_y u$ defines the flow state in state space and evolves according to

$$\partial_t \omega + \mathbf{u} \cdot \nabla \omega = \frac{1}{Re} \nabla^2 \omega - k_f \cos k_f y, \quad (1)$$

where $\mathbf{u} = (u, v)$ is the velocity. In this non-dimensionalisation, the length scale $1/k^* = L^*/2\pi$ is the inverse of the fundamental wavenumber (asterisk denotes dimensional quantities). The time scale is $1/\sqrt{k^* \chi^*}$, where χ^* is the amplitude of the forcing in the momentum equation. The Reynolds number is therefore $Re := \sqrt{\chi^*}/k^{*3}/\nu$, where ν is the kinematic viscosity. The forcing wavenumber is set to $k_f = 4$. Kolmogorov flow approaches an asymptotic regime beyond $Re \approx 50$ [15], and therefore we consider $Re = \{40, 100, 400\}$ in this work. The vorticity-velocity Navier-Stokes equations (1) are solved using the pseudospectral version of the JAX-CFD solver [16, 17], allowing for the efficient computation of gradients of the time-forward map of (1) using automatic differentiation. The computational grid is set to $N_x \times N_y = 128^2$ for $Re = \{40, 100\}$ and 512^2 for $Re = 400$.

Our objective is to estimate the flow state ω_0^* which, when evolved using the Navier-Stokes equations (1), reproduces available measurements $m_n^R = \mathcal{M}(\omega_n^R) \in \mathbb{R}^{d_m}$ from a reference solution ω^R at discrete times $t_n = n\Delta t$ over the time horizon $t_n \in [0, T]$ for $n = 0, \dots, N$. The problem is formulated as a variational minimization of a cost function of the

discrepancy between the estimated and true measurements,

$$\mathcal{J}(\omega_0) = \frac{1}{2} \sum_{n=0}^N \|\mathcal{M}(\omega_n) - m_n^R\|^2, \quad (2)$$

subject to the constraint that $\omega_n = f^{t_n}(\omega_0)$ is the time-forward map of (1) from initial condition ω_0 . The required gradient of (2) with respect to ω_0 can be computed using the discrete adjoint [18] or automatic differentiation [19].

The measurement operator \mathcal{M} is defined to be the coarse-graining operation $\mathcal{M} : \mathbb{R}^{N_x \times N_y} \rightarrow \mathbb{R}^{N_x/M \times N_y/M}$ which samples the high-resolution data at every M^{th} gridpoint in both x - and y -directions. The temporal coarsening $\Delta t = M\delta t$ is set by the same coarsening factor, where δt is the time-step of the numerical simulation. At $Re = \{40, 100\}$, coarsening is set to $M = 16$ and to $M = 64$ at $Re = 400$, resulting in 8^2 spatial measurements for each Re case. The DA time horizon is $T \approx 0.6T_L$ where T_L is the Lyapunov timescale at each Re .

As represented by the blue box in figure 1, the gradient of (2) can be computed by solving the adjoint equations,

$$\frac{\partial \omega^\dagger}{\partial \tau} + J(\psi, \omega^\dagger) - \frac{1}{Re} \nabla^2 \omega^\dagger + \psi^\dagger = \frac{\mathcal{D}\mathcal{J}}{\mathcal{D}\omega}, \quad (3a)$$

$$\nabla^2 \psi^\dagger - J(\omega, \psi^\dagger) = \frac{\mathcal{D}\mathcal{J}}{\mathcal{D}\psi}, \quad (3b)$$

backwards in time, where $\tau := T - t$, as derived in Appendix A. The streamfunction ψ is related to the velocity components via $u = \partial_y \psi$, $v = -\partial_x \psi$, and $J(\psi, \omega) = \frac{\partial \psi}{\partial x} \frac{\partial \omega}{\partial y} - \frac{\partial \psi}{\partial y} \frac{\partial \omega}{\partial x}$. The adjoint field ω^\dagger at $t = 0$ yields the variation of the cost function with respect to the initial condition ω_0 ,

$$\frac{\mathcal{D}\mathcal{J}}{\mathcal{D}\omega_0} = \omega^\dagger(t = 0), \quad (4)$$

which can be used to update the estimated ω_0 in a direction that minimizes the cost by better reproducing the measurements. In lieu of explicit solution of the adjoint equations (3), we compute the gradient (4) by automatic differentiation. The cost function is then minimized using the Adam optimizer [20] for a total of 500 optimization steps at each Re . A sweep over initial step sizes (or learning rates) was performed, such that $\alpha = 0.2$ was selected as the initial step size at each Re .

Variational DA in state space requires a first guess of the initial flow field ω_0 . We will consider two initialization approaches. The first is a bicubic interpolation of the measurements (InterpDA). The second is using a pre-trained super-resolution (SR) network $\mathcal{F}_{SR} : \mathbb{R}^{d_m} \rightarrow \mathbb{R}^{d_\omega}$, which maps from instantaneous measurements to instantaneous full resolution fields. This initialization for data assimilation (SR-DA) was shown to yield significant improvement in the accuracy of the assimilation estimate by Weyrauch *et al.* [11]. The same network as in Page [10] is adopted here, which is trained on the standard L_2 loss between the full resolution snapshot and the super-resolved snapshot. These SR networks were trained with the Adam optimizer with an initial learning rate of 10^{-4} and a batch size of 32, on data sets of 5000 turbulent snapshots at each Re for a total of 250 epochs. Full details on the data generation is given in Appendix C. These assimilations in state space serve as a benchmark for the proposed latent-space assimilation.

III. LATENT-SPACE DATA ASSIMILATION

The classical variational-DA algorithm attempts to identify the optimal initial vorticity, or state-space representation of the flow, to reproduce the measurement. The main idea of our latent-space DA is to, instead, attempt to predict a latent-space representation $\eta \in \mathbb{R}^{d_\eta}$ (see the orange box in figure 1). Shifting the object of the optimization to the latent space requires an evaluation of the gradient with respect to the new latent coordinates. The latent space is mapped to state space by a pre-trained decoder $\mathcal{F}_D(\eta) = \omega \in \mathbb{R}^{d_\omega}$. The new DA cost function is then

$$\mathcal{J}(\eta_0) = \frac{1}{2} \sum_{n=0}^N \|\mathcal{M} \circ f^{t_n} \circ \mathcal{F}_D(\eta_0) - m_n^R\|^2, \quad (5)$$

where the latent state estimate η_0 is first decoded to state space, then (1) is solved in state space and finally the model observations are compared to available measurements (combined orange and blue boxes in figure 1). The adjoints in latent and state space are related by the Jacobian $\partial \mathcal{F}_D / \partial \eta \in \mathbb{R}^{d_\omega \times d_\eta}$,

$$\eta^\dagger = \left(\frac{\partial \mathcal{F}_D}{\partial \eta} \right)^\top \omega^\dagger. \quad (6)$$

We note that no dynamical model in the latent space is required and all time marching is performed in state space, such that the estimated solution $f^t(\mathcal{F}_{\mathcal{D}}(\eta_0))$ for $t \in [0, T]$ exactly satisfies the Navier-Stokes equations (1). Furthermore, given a pre-existing adjoint solver for the flow in question, only the ability to compute vector-Jacobian products of the decoder is required to perform latent-space DA according to (6). As in state-space DA, the Adam optimizer is used to minimize (5), and the same number of optimization steps were taken. A sweep over initial step sizes led to the choices $\alpha = \{5, 0.2, 0.02\}$ at $Re = \{40, 100, 400\}$.

A. The latent space

We adopt the latent space of the implicit rank-minimizing autoencoder (IRMAE). Unlike standard autoencoders, IRMAE is distinguished by the addition of a series of fully-connected, linear layers in the bottleneck of the network, which drive down the intrinsic dimensionality of the latent representation [5, 21]. The IRMAE architecture has demonstrated comparable performance to variational autoencoders for smooth interpolation in the latent space and generating new samples from random noise [21]. As such, the latent representation exhibits these favorable properties in addition to being approximately minimal rank.

The IRMAE network \mathcal{A} seeks to learn the identity function

$$\mathcal{A}(\omega) \equiv [\mathcal{F}_{\mathcal{D}} \circ \mathcal{W} \circ \mathcal{F}_{\mathcal{E}}](\omega) \approx \omega, \quad (7)$$

where the encoder $\mathcal{F}_{\mathcal{E}} : \mathbb{R}^{d_{\omega}} \rightarrow \mathbb{R}^{d_{\eta}}$ maps the input vorticity snapshot to a low-dimensional representation ($d_{\eta} = 1024$), $\mathcal{W} : \mathbb{R}^{d_{\eta}} \rightarrow \mathbb{R}^{d_{\eta}}$ represents a series of four fully-connected, equally-sized linear layers (pure matrix multiplication) within the embedding space, and the decoder $\mathcal{F}_{\mathcal{D}}$ is defined as above. The encoder and decoder consist of a series of convolutional dense blocks at varying resolutions.

To train the networks at $Re = \{40, 100, 400\}$, datasets were generated by sampling long-time trajectories of the flow at every time unit, resulting in datasets with a total number of snapshots $N_S \approx \{6, 10, 10\} \times 10^4$, respectively. Initial transient periods of 50 time units were discarded from the trajectories, such that the training data is sampled from the turbulent attractor. The networks are then trained to minimize the loss function

$$\mathcal{L} = \frac{1}{N_S} \sum_{j=1}^{N_S} \|\mathcal{A}(\omega^j) - \omega^j\|^2, \quad (8)$$

where each ω^j is a full-field snapshot from the training dataset. Full details of the IRMAE architecture and training protocol and reconstruction accuracy of (7) are provided in Appendices B and C, respectively. For each Re considered, DA was performed on independent trajectories which were never seen during the training of the neural networks.

Variational DA in latent space requires an first guess of the initial latent representation η_0 . This initialization is obtained by using the aforementioned pre-trained SR network followed by the IRMAE encoder, i.e., $\eta_0 = \mathcal{F}_{\mathcal{E}} \circ \mathcal{F}_{SR}(m_0^R)$. Comparable performance can be achieved by training a fully-connected network to map directly from measurement space to the IRMAE latent space.

IV. RESULTS

A. Accuracy of the estimated fields

The accuracy of the flow trajectories is compared when the initial flow states are estimated from a single inference of the super-resolution network (SR), super-resolution-initialized DA in state space (SR-DA), and DA in latent space (LatentDA). Standard state-space DA initialized with a bicubic interpolation (InterpDA) is presented as a benchmark. The evolution of the error,

$$\varepsilon(t) = \|f^t(\omega_0^*) - f^t(\omega_0^R)\| / \|f^t(\omega_0^R)\|, \quad (9)$$

for each method at $Re = \{40, 100, 400\}$ is reported in figure 2, where ω_0^* and ω_0^R are the estimated and reference turbulent fields at $t = 0$. The spatio-temporal coarsening factor was $M = 16$ at both $Re = \{40, 100\}$ and $M = 64$ at $Re = 400$, and DA was performed over the time horizon $T \approx 0.6T_L$ which is indicated by the gray shaded region in figure 2.

LatentDA (red) results in an improvement of approximately two orders of magnitude over the standard InterpDA approach (blue) and one order of magnitude over SR-DA (green) at $Re = \{40, 100\}$. Even at $Re = 400$, we still observe

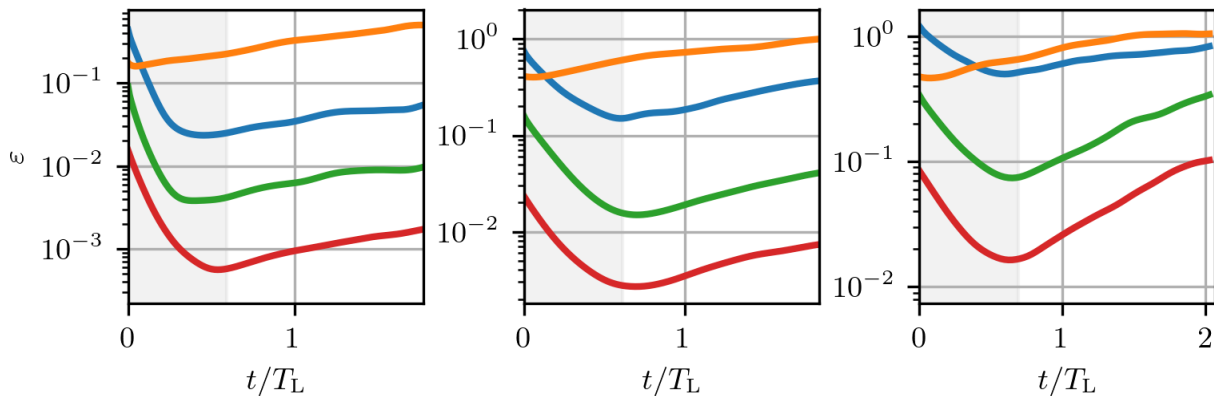


FIG. 2. Relative error ε of the estimated turbulent field by (blue) InterpDA, (orange) SR, (green) SR-DA and (red) LatentDA at (left) $Re = 40$, (middle) $Re = 100$ and (right) $Re = 400$ as a function of time normalized by the Lyapunov timescale. Bold colored lines: ensemble mean of ten independent trajectories. Gray region marks the data-assimilation time horizon.

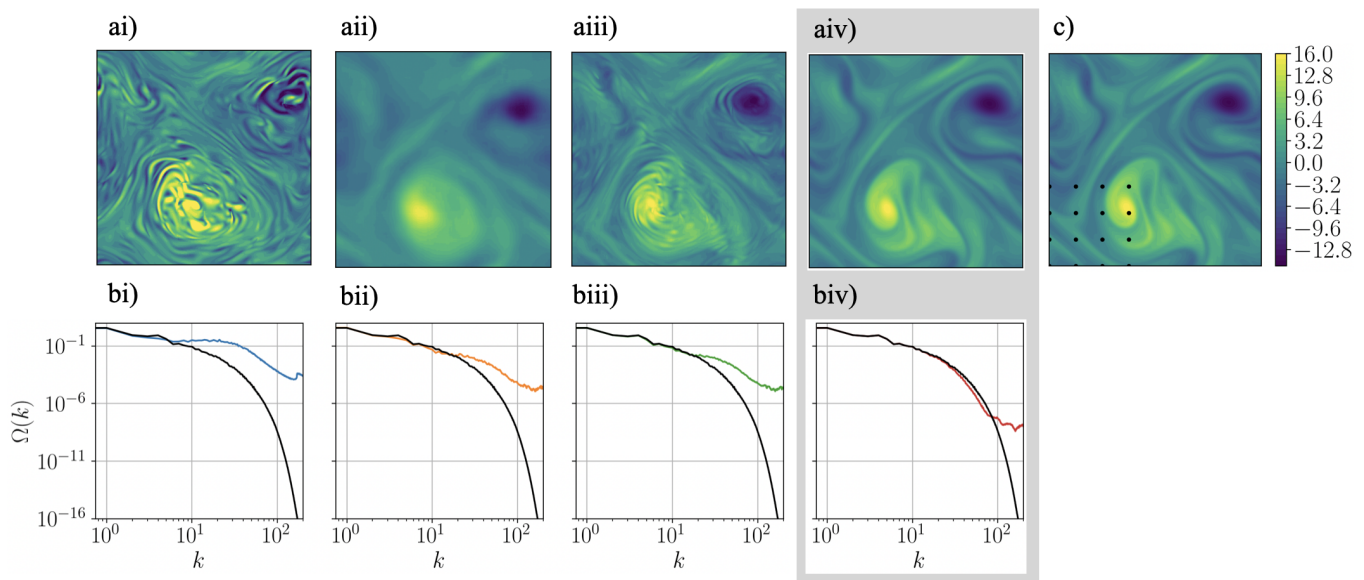


FIG. 3. Comparison of the estimated field ω_0^* from (i-iv) InterpDA, SR, SR-DA and LatentDA (highlighted by gray box) with (c) reference ω_0^R at $t = 0$ at $Re = 400$. The lattice of black dots in (c) indicates the sensor resolution. (b) Enstrophy spectra $\Omega(k)$ as a function of wavenumber k . The black spectra denote the reference data.

an improvement by more than one order of magnitude over the InterpDA approach, and a significant reduction of $\sim 50\%$ error over the best-performing approach in state space (SR-DA). Furthermore, table I reveals that the standard deviation of the percent relative error at the DA time horizon T using LatentDA is significantly smaller than SR-DA at $Re = 400$. Since the accuracy advantage of the estimated trajectories from LatentDA is retained throughout the observation horizon, and because the growth rate of $\varepsilon(t)$ after $t = T$ is consistent across all three DA approaches, accurate predictions from LatentDA can be made over much longer time intervals. For example, at $Re = 100$ and

Re	InterpDA	SR	SR-DA	LatentDA
40	2.5 ± 1.7	22.4 ± 6.5	0.4 ± 0.8	0.06 ± 0.04
100	15.0 ± 19.2	60.7 ± 4.4	1.6 ± 0.3	0.28 ± 0.04
400	51.6 ± 25.8	65.5 ± 6.8	7.5 ± 4.2	1.70 ± 1.10

TABLE I. Mean and standard deviation of the percent relative error ($\varepsilon \times 100$) of the estimated turbulent field at the DA time horizon $t = T$, over an ensemble of ten independent trajectories.

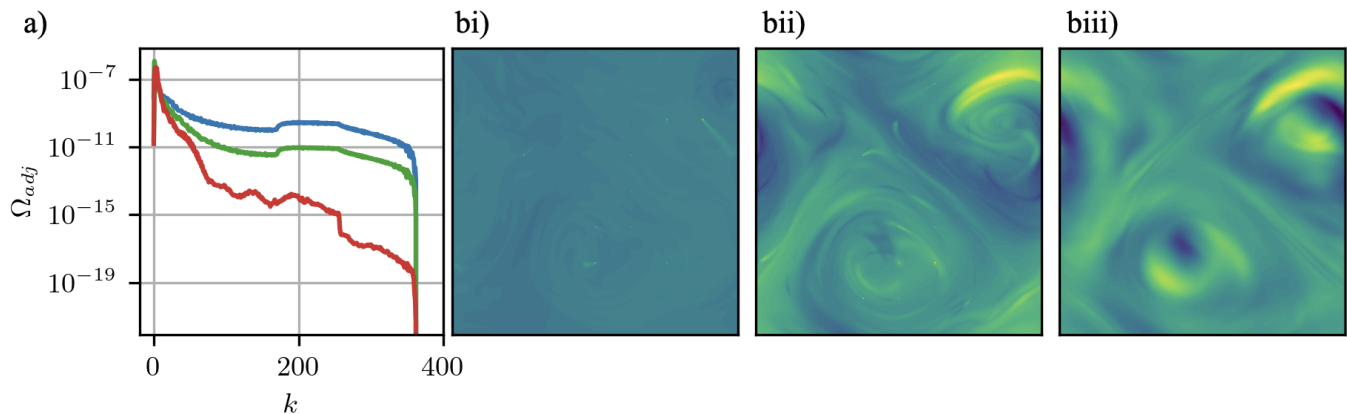


FIG. 4. (a) The spectra Ω_{adj} of the initial normalized adjoint field in state space ω^\dagger for (blue) InterpDA, (green) SR-DA and (red) LatentDA adjoint field decoded to state space $\mathcal{F}_{\mathcal{D}}(\eta + \alpha\eta^\dagger) - \mathcal{F}_{\mathcal{D}}(\eta)$ at $Re = 400$. Contours of the state-space adjoint for InterpDA (bi), SR-DA (bii) and (biii) decoded LatentDA adjoint fields.

using LatentDA, the prediction error is $\sim 1\%$ at $2.5T_L$ (not shown), which is a four folds longer horizon than when using SR-DA.

A comparison of the estimated ω_0^* fields at $Re = 400$ using each approach is presented in figure 3. When the data is assimilated in state space (figure 3i), ω_0^* exhibits unphysical high-wavenumber artifacts and does not at all resemble the reference data (figure 3c). In contrast, the estimated field by SR (figure 3ii) is overly smooth, which is a symptom of the spectral bias of neural networks. State-space DA initialized with this field (SR-DA) introduces some high-frequency errors (figure 3iii), but the enstrophy spectrum $\Omega(k)$ remains poorly representative of the true field. When the assimilation is performed in latent space (figure 3iv, highlighted by the gray box), the predicted initial field is most accurate and $\Omega(k)$ is most consistent with the reference turbulent state. Similar trends were observed at the lower Re considered.

To understand the cause of the high-wavenumber artifacts in state-space DA, it should be noted that the adjoint equations (3) are forced by $\mathcal{D}\mathcal{J}/\mathcal{D}\omega$, which is a series of singular impulses in space and time at each measurement location. These superpositions of delta functions are advected and diffused by (3), but signatures of this forcing are very apparent in the visualization of $\omega^\dagger(t=0)$ at $Re = 400$ in figures 4(bi,bii). As the Fourier transform of a delta function is a constant function of k , these singular impulses lead to high wavenumber spectral content of the state-space adjoint variables (figure 4a). Each variational DA iteration slightly perturbs the turbulent field estimate in a direction with high energy in the high wavenumbers. For latent-DA, the effective adjoint update can be visualized in state space by evaluating $\mathcal{F}_{\mathcal{D}}(\eta + \alpha\eta^\dagger) - \mathcal{F}_{\mathcal{D}}(\eta)$. As shown in figure 4, the energy in the high wavenumbers of this effective latent adjoint direction is many orders of magnitude smaller than the state-space adjoint directions, which is consistent with the improved spectrum of ω_0^* for LatentDA. Adjoint directions are normalized before their spectra are computed to enable comparison between state space and latent space.

B. Robustness to noisy measurements

In practice, the measurement data available for assimilation are typically not perfect, but rather corrupted by some sensor error. We briefly investigate the effect of measurement noise on LatentDA as a test of the robustness of the proposed method. Similarly to Wang and Zaki [22] and Page [10], noise is added to the measurements of the reference trajectories

$$m_{n,j}^R \leftarrow m_{n,j}^R + \Sigma_{n,j}, \quad (10)$$

where $m_n^R = \{m_{n,j}^R\}_{j=1}^{N_x N_y / M^2}$ are the measurements at each discrete time t_n , and the noise is normally distributed based on the local absolute vorticity $\Sigma_{n,j} \sim \mathcal{N}(0, \sigma |m_{n,j}^R|)$. We consider noise amplitudes of $\sigma \in \{0, 0.05, 0.1\}$, and the same noise is also present when initializing each variational procedure, whether by interpolation (InterpDA) or by a pre-trained SR network inference (SR, SR-DA and LatentDA).

The relative error of the estimated turbulent state at the initial time $t = 0$ and at the DA time horizon $t = T$ are reported as a function of σ in figure 5 for $Re = 400$. All methods are similarly robust to the increasing noise

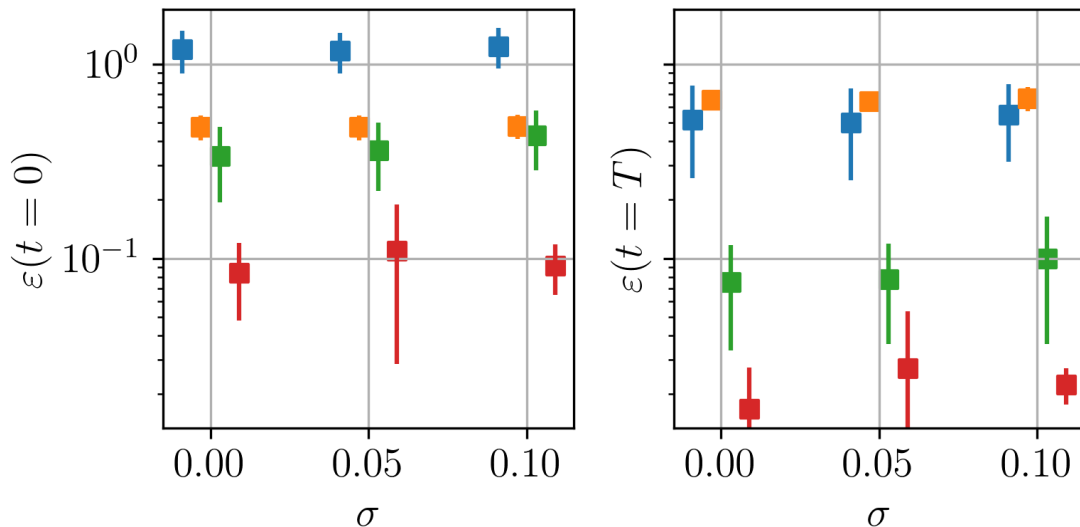


FIG. 5. Relative error of the estimated turbulent field at (left) the initial time $\varepsilon(t=0)$ and (right) the DA time horizon $\varepsilon(t=T)$ as a function of the noise amplitude σ , by (blue) InterpDA, (orange) SR, (green) SR-DA and (red) LatentDA at $Re = 400$ (markers are slightly offset for clarity).

at both times considered. As such, LatentDA maintains its reconstruction accuracy advantage over all state-space assimilation methods when measurements are noisy. This is a promising result in the context of scaling LatentDA to higher- Re , experimental measurements.

C. Observability in latent space

We consider two dynamical perspectives that explain the improved performance of LatentDA. The first perspective recalls that the IRMAE models have been trained on data sampled from the turbulent attractor $\omega \in \mathcal{A}$ and have learned latent representations η such that $\mathcal{F}_{\mathcal{D}}(\eta) \in \mathcal{A}$ holds approximately. Let us consider the gradient direction in latent space, $\alpha\eta^\dagger$, as a small perturbation such that $\mathcal{F}_{\mathcal{D}}(\eta - \alpha\eta^\dagger) \in \mathcal{A}$ still holds approximately. By expanding this small perturbation to linear order,

$$\mathcal{F}_{\mathcal{D}}(\eta - \alpha\eta^\dagger) = \mathcal{F}_{\mathcal{D}}(\eta) - \alpha \frac{\partial \mathcal{F}_{\mathcal{D}}}{\partial \eta} \eta^\dagger + \dots \in \mathcal{A},$$

it is clear that the columns of the decoder Jacobian are the perturbation directions which, to linear order, approximately remain on the turbulent attractor. The linear transformation of adjoints from state to latent space (6) can now be understood as a projection onto these physically relevant perturbation directions. The associated linearized update in state space is given by,

$$\omega_0^* \approx \mathcal{F}_{\mathcal{D}}(\eta) - \alpha \frac{\partial \mathcal{F}_{\mathcal{D}}}{\partial \eta} \left(\frac{\partial \mathcal{F}_{\mathcal{D}}}{\partial \eta} \right)^\top q^\dagger.$$

As such, the estimate remains physically relevant in state space throughout the latent variational DA method, to linear order. Physically, these improved perturbation directions are marked by an absence of the high-wavenumber artifacts discussed previously.

The second perspective considers how observable the reference initial turbulent field is from the measurements. As we will show here, the iterative gradient-based updates throughout the variational DA method are also expansions in some basis of adjoint fields. When assimilating data variationally, it is beneficial for the reference turbulent field ω_0^R to be well represented in this basis, such that the iterative updates can more effectively converge onto ω_0^R . To begin, we define the deviation field $w = \omega - \omega^R$ which is governed by the linearized Navier-Stokes equations

$$\partial_t w - J(\varphi, \omega^R) - J(\psi^R, w) = \frac{1}{Re} \nabla^2 w, \quad (11)$$

with the associated deviation streamfunction $\varphi = -\nabla^2 w$ and the ground truth streamfunction $\psi^R = -\nabla^2 \omega^R$. As shown in Wang *et al.* [23] for turbulent channel flow, the DA cost function (2) can be written in terms of the measurement kernel $\phi(\mathbf{x}_m)$ which extracts the measurement of interest at location \mathbf{x}_m

$$\mathcal{J}(w_0) = \frac{1}{2} \sum_{n=0}^N \sum_{m=1}^{d_m} \langle w(t = t_n), \phi(\mathbf{x}_m) \rangle^2, \quad (12)$$

where $\langle a, b \rangle = \int_V ab \, dV$ is the spatial inner product over the computational domain V . In this study $\phi(\mathbf{x}_m) = \delta(\mathbf{x} - \mathbf{x}_m)$ is the Kronecker delta function, but more complex kernels can be defined as required. Forward-adjoint duality can be exploited to write (12) in terms of the adjoint field w^\ddagger , as

$$\begin{aligned} \langle w(t = t_n), \phi(\mathbf{x}_m) \rangle &= \langle \mathcal{L}w_0, \phi(\mathbf{x}_m) \rangle \\ &= \langle w_0, \mathcal{L}^\ddagger \phi(\mathbf{x}_m) \rangle \\ &= \langle w_0, w^\ddagger(t = 0; t = t_n, \mathbf{x}_m) \rangle, \end{aligned}$$

where \mathcal{L} is the forward operator of the linearized Navier-Stokes equations (11) which advances w_0 to $w(t = t_n)$. Note that $w^\ddagger \neq \omega^\ddagger$, and an explicit relation between them will be given below. The associated adjoint operator \mathcal{L}^\ddagger solves the linearized adjoint equations

$$\frac{\partial w^\ddagger}{\partial \tau} + J(\psi^R, w^\ddagger) - \frac{1}{Re} \nabla^2 w^\ddagger + \varphi^\ddagger = 0, \quad (13a)$$

$$\nabla^2 \varphi^\ddagger - J(\omega^R, w^\ddagger) = 0, \quad (13b)$$

with the initial condition $w^\ddagger(\tau = 0) = \phi(\mathbf{x}_m)$. This duality can be used to rewrite (12) as

$$\mathcal{J}(w_0) = \frac{1}{2} \sum_{n=0}^N \sum_{m=1}^{d_m} \langle w_0, w^\ddagger(t = 0; t = t_n, \mathbf{x}_m) \rangle^2, \quad (14)$$

enabling the explicit expression of the gradient and the Hessian of the DA cost function,

$$\omega^\dagger(t = 0) = \frac{\mathcal{D}\mathcal{J}}{\mathcal{D}w_0} = \sum_{n=0}^N \sum_{m=1}^{d_m} \langle w_0, w^\ddagger(t = 0; t = t_n, \mathbf{x}_m) \rangle w^\ddagger(t = 0; t = t_n, \mathbf{x}_m), \quad (15)$$

$$\mathcal{H} := \frac{\mathcal{D}^2\mathcal{J}}{\mathcal{D}w_0\mathcal{D}w_0} = \sum_{n=0}^N \sum_{m=1}^{d_m} w^\ddagger(t = 0; t = t_n, \mathbf{x}_m) w^\ddagger(t = 0; t = t_n, \mathbf{x}_m). \quad (16)$$

The gradient (15) is then an expansion in the basis spanned by the adjoint fields $w^\ddagger(t = 0; t = t_n, \mathbf{x}_m)$, while the Hessian (16) can be written as the cross-correlation $\mathcal{H} = AA^\top$ of the matrix A with these adjoint fields as columns. In state space, \mathcal{H} is computed at the estimated ω_0^* , and in latent space $\mathcal{H} = \mathcal{D}^2\mathcal{J}/\mathcal{D}\eta_0\mathcal{D}\eta_0$ is computed at the estimated η_0^* .

The eigendecomposition $\mathcal{H}v_i = \lambda_i v_i$ with eigenvalues λ_i and eigenvectors v_i then yields a proper orthogonal decomposition (POD) basis for these adjoint fields. We examine how well the ground truth turbulent state ω_0^R can be represented in this adjoint basis by computing its reconstruction at $t = 0$ using the first i POD modes of the Hessian at ω_0^* ,

$$\omega_{0,i}^R = \sum_{j=0}^i \langle v_j, \omega_0^R \rangle v_j. \quad (17)$$

The relative error ε of the reconstruction is reported in figure 6, for $Re = 100$, where we compare SR-DA (green) and η_0^* obtained with LatentDA (red). The first 500 adjoint POD modes were computed by the Arnoldi iteration. The reconstructions were also time-evolved over the DA time horizon, and the time-averaged relative errors (circles) were computed as a function of the number of adjoint POD modes used. The reference turbulent state can be reconstructed to $\sim 5\%$ relative error in the latent adjoint basis with 500 adjoint POD modes, as opposed to $\sim 50\%$ relative error in the state-space adjoint basis, demonstrating the improved observability of ω_0^R from the measurements in the latent space near optimality. Perhaps more notably, ~ 100 modes in latent space can reconstruct the reference turbulent state

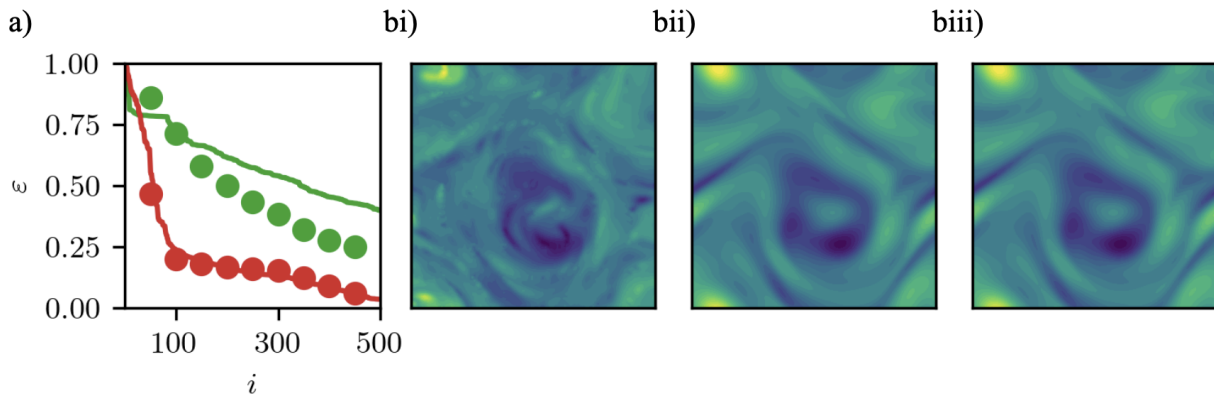


FIG. 6. (a) The relative error ε of the instantaneous reconstruction of the reference turbulent field $\omega_{0,i}^R$ (lines) and the time-averaged relative error over the DA time horizon (circles) using the first i adjoint POD modes in (green) state and (red) latent space at $Re = 100$. (b) Contours of the out-of-plane vorticity of the reconstructed field with 500 adjoint POD modes in (i) state and (ii) latent space, and (iii) the reference turbulent field.

with $\sim 20\%$ error, while the same number of modes can only reconstruct the state with $\sim 75\%$ error in state space. High wavenumber artifacts and signatures of the localized adjoint forcing are evident in the state-space adjoint basis reconstruction (figure 6bi). These small-scale fluctuations decay over the DA time horizon, explaining the improved time-averaged relative errors in state space. In contrast, the decoded reconstruction in latent space very closely resembles the reference turbulent state (panels bii-biii), and the error in the representation of the initial state and the time-averaged errors during the evolution are similar. These results demonstrate that the observability of the turbulence using limited measurements can be appreciably improved when the assimilation is performed in the right space, or coordinates.

V. CONCLUSION

In the study of turbulence, we often rely on the interpretation of measurements to probe the dynamics of the underlying flow. Data assimilation seeks to map from the measurements to the associated turbulent state that satisfies the Navier-Stokes equations. We ask the question if our ability to observe the turbulence can be significantly improved by first mapping from the measurements to a pre-designed latent space, and subsequently to the full turbulent field? We demonstrate that the mapping to the latent intermediate coordinates, namely the latent space of a pre-trained autoencoder, can lead to significant accuracy improvement in the interpretation of turbulence measurements.

In state-space DA, the adjoint field is highly localized in the vicinity of the delta-function forcing, such that the spectrum of the adjoint field is broadband. The updates in latent space are more targeted and physically relevant, resulting in more accurate reconstruction of both the large and small scales, and a smaller departure from the truth over time. An improvement of an order of magnitude was achieved when assimilating data in latent space at $Re = 40$ and 100, compared to the best approach considered in state space. A lower but nonetheless appreciable improvement was achieved at $Re = 400$, where the increased spatiotemporal complexity of the flow requires a larger latent space dimensionality. The small scales of the estimated flow state are more dynamically relevant at all Re considered. LatentDA also exhibited a comparable robustness to noisy measurements as all state-space DA methods.

This work demonstrates the potential benefits of combining variational and data-driven techniques to interpret turbulence measurements. The observability of turbulence from the data is much improved by taking advantage of the latent space of the autoencoder. More generally, the results demonstrate the power of exploiting such new latent spaces in the study of turbulence.

Appendix A: Continuous adjoint equations: vorticity-streamfunction formulation

The 2D velocity-vorticity Navier-Stokes equations (1) with some forcing g can be written in terms of the vorticity and streamfunction ψ as

$$\frac{\partial \omega}{\partial t} - J(\psi, \omega) - \frac{1}{Re} \nabla^2 \omega + g = 0, \quad (\text{A1})$$

where

$$J(\psi, \omega) = \frac{\partial \psi}{\partial x} \frac{\partial \omega}{\partial y} - \frac{\partial \psi}{\partial y} \frac{\partial \omega}{\partial x} \quad (\text{A2})$$

and ψ is related to the velocity components via $u = \partial_y \psi, v = -\partial_x \psi$, such that ψ is recovered from ω by solving the Poisson equation $\nabla^2 \psi = -\omega$. The constrained optimization problem (2) can be cast as an unconstrained optimization problem by defining the Lagrangian

$$\mathcal{L} = \mathcal{J} - \left(\omega^\dagger, \frac{\partial \omega}{\partial t} - J(\psi, \omega) - \frac{1}{Re} \nabla^2 \omega + g \right) - \left(\psi^\dagger, \omega + \nabla^2 \psi \right), \quad (\text{A3})$$

where the inner product is defined by integrating over space V and the observation time horizon $t \in [0, T]$

$$(a, b) = \int_0^T \int_V ab \, dV dt. \quad (\text{A4})$$

Taking variations of \mathcal{L} with respect to the Lagrange multipliers ω^\dagger and ψ^\dagger yields the Navier-Stokes equation for the estimated ω and the Poisson equation relating ω to ψ . To take variations of \mathcal{L} with respect to ω and ψ , we proceed as follows. Assuming periodic boundary conditions, one can re-express terms such as $(\omega^\dagger, J(\psi, \omega))$ by integrating by parts in space

$$\begin{aligned} (\omega^\dagger, J(\psi, \omega)) &= \int_0^T \int_V \omega^\dagger \left[\frac{\partial \psi}{\partial x} \frac{\partial \omega}{\partial y} - \frac{\partial \psi}{\partial y} \frac{\partial \omega}{\partial x} \right] dV dt, \\ &= \iint \left[\frac{\partial}{\partial x} \left(\omega^\dagger \frac{\partial \psi}{\partial y} \right) \omega - \frac{\partial}{\partial y} \left(\omega^\dagger \frac{\partial \psi}{\partial x} \right) \omega \right] dV dt, \\ &= - \left(J(\psi, \omega^\dagger), \omega \right), \end{aligned}$$

where in the final equality, we assume commutativity of the partial derivatives. By the antisymmetry of J , the relation $(\omega^\dagger, J(\psi, \omega)) = (J(\omega, \omega^\dagger), \psi)$ follows quickly. By isolating ω in the remaining terms, the Lagrangian (A3) can be written as

$$\begin{aligned} \mathcal{L} &= \mathcal{J} - \omega^\dagger(T)\omega(T) + \omega^\dagger(0)\omega_0 \\ &\quad + \left(\frac{\partial \omega^\dagger}{\partial t} - J(\psi, \omega^\dagger) + \frac{1}{Re} \nabla^2 \omega^\dagger - \psi^\dagger, \omega \right) \\ &\quad - \left(\omega^\dagger, g \right) - \left(\nabla^2 \psi^\dagger, \psi \right). \end{aligned} \quad (\text{A5})$$

Taking variations of \mathcal{L} with respect to ω is now straightforward, and variations with respect to ψ follow quickly from the antisymmetry of J . Setting $\mathcal{D}\mathcal{L}/\mathcal{D}\omega = 0$ and $\mathcal{D}\mathcal{L}/\mathcal{D}\psi = 0$ yields the equations for the adjoint fields ω^\dagger and ψ^\dagger

$$\frac{\partial \omega^\dagger}{\partial \tau} + J(\psi, \omega^\dagger) - \frac{1}{Re} \nabla^2 \omega^\dagger + \psi^\dagger = \frac{\mathcal{D}\mathcal{J}}{\mathcal{D}\omega}, \quad (\text{A6})$$

$$\nabla^2 \psi^\dagger - J(\omega, \omega^\dagger) = \frac{\mathcal{D}\mathcal{J}}{\mathcal{D}\psi}, \quad (\text{A7})$$

where $\tau = T - t$ is the backwards time. Then, the adjoint field at $t = 0$ yields the total variation of the cost function with respect to the initial condition ω_0 ,

$$\frac{\mathcal{D}\mathcal{J}}{\mathcal{D}\omega_0} = \omega^\dagger(t = 0). \quad (\text{A8})$$

Appendix B: IRMAE architecture

1. $Re = 40$ & 100

The IRMAE architecture used at $Re = 40$ and 100 is adopted from Cleary and Page [6]. Dense blocks (DB) [24] are groups of convolutional layers where the output of each layer is concatenated with its input. Here, each dense block is

made up of three convolutional layers, each with 32 filters. We apply the ‘GELU’ activation function [25] and batch normalization [26] to the output of convolutional layers. The encoder architecture is given by the following sequence of operations:

$$\begin{aligned}
\omega &\rightarrow \text{PC}(8 \times 8, 32) \rightarrow \text{DB}(8 \times 8) \rightarrow \text{MP}(2 \times 2) \\
&\rightarrow \text{PC}(4 \times 4, 32) \rightarrow \text{DB}(4 \times 4) \rightarrow \text{MP}(2 \times 2) \\
&\rightarrow \text{PC}(4 \times 4, 32) \rightarrow \text{DB}(4 \times 4) \rightarrow \text{MP}(2 \times 2) \\
&\rightarrow \text{PC}(4 \times 4, 32) \rightarrow \text{DB}(4 \times 4) \\
&\rightarrow \text{PC}(4 \times 4, 4) \rightarrow \text{Flatten} = \mathcal{F}_{\mathcal{E}}(\omega),
\end{aligned} \tag{B1}$$

where ‘PC’ stands for a convolutional layer with periodic padding and ‘MP’ for a max pooling layer. The first term in the brackets denotes the size of the convolutional filters and the second term denotes the number of filters.

The bottleneck \mathcal{W} consists of a series of four fully connected (‘FC’) linear layers with equal input/output dimension,

$$\mathcal{F}_{\mathcal{E}}(\omega) \rightarrow \text{FC}(1024)^4 = \mathcal{W}(\mathcal{F}_{\mathcal{E}}(\omega)). \tag{B2}$$

The latent space is the output of this bottleneck, which is then reshaped into an image with four channels of dimension 16^2 . The decoder then mirrors the encoder, with the addition of an output stream of linear periodic convolutional layers (‘LPC’):

$$\begin{aligned}
\mathcal{W}(\mathcal{F}_{\mathcal{E}}(\omega)) &\rightarrow \text{Reshape} \\
&\rightarrow \text{PC}(4 \times 4, 32) \rightarrow \text{DB}(4 \times 4) \rightarrow \text{UP}(2 \times 2) \\
&\rightarrow \text{PC}(4 \times 4, 32) \rightarrow \text{DB}(4 \times 4) \rightarrow \text{UP}(2 \times 2) \\
&\rightarrow \text{PC}(4 \times 4, 32) \rightarrow \text{DB}(4 \times 4) \rightarrow \text{UP}(2 \times 2) \\
&\rightarrow \text{PC}(8 \times 8, 32) \rightarrow \text{DB}(8 \times 8) \\
&\rightarrow \text{LPC}(16 \times 16, 1) \rightarrow \text{LPC}(12 \times 12, 1) \\
&\rightarrow \text{LPC}(8 \times 8, 1) \rightarrow \text{LPC}(6 \times 6, 1) \\
&= \mathcal{F}_{\mathcal{D}}(\mathcal{W}(\mathcal{F}_{\mathcal{E}}(\omega))) = \mathcal{A}(\omega),
\end{aligned} \tag{B3}$$

where ‘UP’ denotes upsampling layers.

2. $Re = 400$

The architecture of IRMAE at $Re = 400$ was slightly modified from that used at $Re = 40$ and 100, such that the input and output vorticity fields would be of resolution 512×512 . One extra downsampling/upsampling operation was inserted into the encoder/decoder, such that the input field was reduced to have dimension 32^2 , rather than 16^2 . The kernel sizes were also modified throughout the encoder and decoder to reflect the increased dimensionality of the input/output vorticity fields, as outlined below.

The encoder architecture is given by the following sequence of operations:

$$\begin{aligned}
\omega &\rightarrow \text{PC}(8 \times 8, 32) \rightarrow \text{DB}(8 \times 8) \rightarrow \text{MP}(2 \times 2) \\
&\rightarrow \text{PC}(8 \times 8, 32) \rightarrow \text{DB}(8 \times 8) \rightarrow \text{MP}(2 \times 2) \\
&\rightarrow \text{PC}(8 \times 8, 32) \rightarrow \text{DB}(8 \times 8) \rightarrow \text{MP}(2 \times 2) \\
&\rightarrow \text{PC}(4 \times 4, 32) \rightarrow \text{DB}(4 \times 4) \rightarrow \text{MP}(2 \times 2) \\
&\rightarrow \text{PC}(4 \times 4, 32) \rightarrow \text{DB}(4 \times 4) \\
&\rightarrow \text{PC}(4 \times 4, 1) \rightarrow \text{Flatten} = \mathcal{F}_{\mathcal{E}}(\omega),
\end{aligned} \tag{B4}$$

The input vorticity field is a single-channel image of size 512^2 , hence the output of the encoder $\mathcal{F}_{\mathcal{E}}(\omega)$ is a flattened vector of length $32^2 = 1024$.

The architecture of the bottleneck is unchanged from the lower Re bottleneck architecture. The latent representation

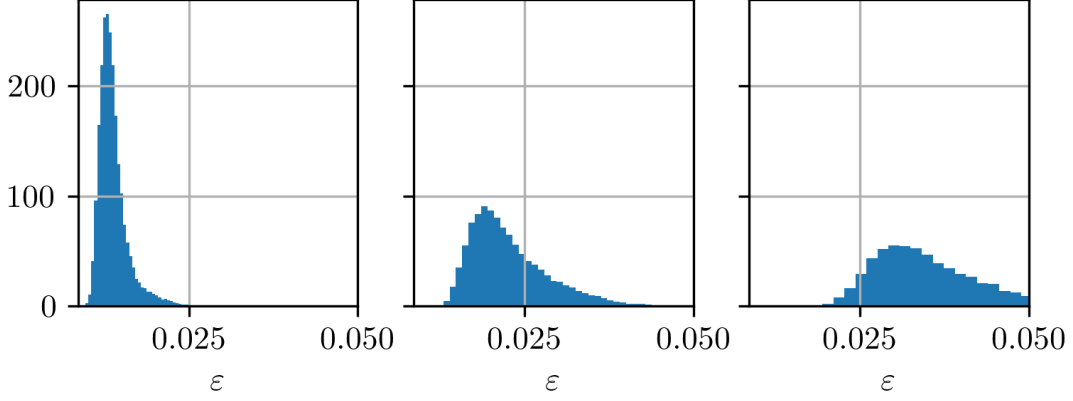


FIG. 7. PDFs of the relative reconstruction error of IRMAE at $Re = 40, 100$ and 400 , from left to right.

is then reshaped to have dimension 32^2 . The decoder architecture is again slightly modified to mirror the encoder,

$$\begin{aligned}
 \mathcal{W}(\mathcal{F}_{\mathcal{E}}(\omega)) &\rightarrow \text{Reshape} \\
 &\rightarrow \text{PC}(4 \times 4, 32) \rightarrow \text{DB}(4 \times 4) \rightarrow \text{UP}(2 \times 2) \\
 &\rightarrow \text{PC}(4 \times 4, 32) \rightarrow \text{DB}(4 \times 4) \rightarrow \text{UP}(2 \times 2) \\
 &\rightarrow \text{PC}(8 \times 8, 32) \rightarrow \text{DB}(8 \times 8) \rightarrow \text{UP}(2 \times 2) \\
 &\rightarrow \text{PC}(8 \times 8, 32) \rightarrow \text{DB}(8 \times 8) \rightarrow \text{UP}(2 \times 2) \\
 &\rightarrow \text{PC}(8 \times 8, 32) \rightarrow \text{DB}(8 \times 8) \\
 &\rightarrow \text{LPC}(16 \times 16, 1) \rightarrow \text{LPC}(12 \times 12, 1) \\
 &\rightarrow \text{LPC}(8 \times 8, 1) \rightarrow \text{LPC}(6 \times 6, 1) \\
 &= \mathcal{F}_{\mathcal{D}}(\mathcal{W}(\mathcal{F}_{\mathcal{E}}(\omega))) = \mathcal{A}(\omega).
 \end{aligned} \tag{B5}$$

Appendix C: Data Generation and IRMAE training

Datasets were generated at each Re by sampling long trajectories of the flow. At $Re = \{40, 100\}$, 100 trajectories of length 10^3 were sampled at every advective time unit. Initial transient periods of 50 time units were discarded from the trajectories, such that the training data is sampled from the turbulent attractor. The resulting dataset was resampled according to the dissipation rate of each snapshot, as in Cleary and Page [6].

The $Re = 40$ and 100 networks were initialized with the final network weights from Cleary and Page [6], which were trained on symmetry-reduced snapshots (both continuous and discrete symmetries of Kolmogorov flow). We refer the reader to Cleary and Page [6] for full details on the training hyperparameters, symmetry reduction protocol and reconstruction error of these network weights.

However, we do not assume that the measurements are taken from symmetry-reduced turbulent states here, so these network weights are further fine-tuned on data which is augmented at every epoch with random symmetry operations. The AdamW optimizer [27] is used for this transfer learning, with an initial learning rate of 10^{-4} and the default weight decay coefficient of 0.004 for 500 epochs.

At $Re = 400$, four trajectories of length 2.5×10^4 were sampled at every time unit, resulting in $N_S = 10^5$ snapshots. Again, initial transient periods of 50 time units were discarded from these trajectories. These snapshots were not resampled according to dissipation rate, as i) it is more computationally expensive to generate large datasets at the increased Re and increased resolution of 512^2 and ii) the dissipation rate distribution is less skewed at the higher Re .

The $Re = 400$ IRMAE network was trained from scratch to input/output states on the finer computational grid of 512^2 . The AdamW optimizer is used with an initial learning rate of 10^{-4} and the default weight decay coefficient of 0.004 for 400 epochs. The training data is symmetry augmented at every epoch with random symmetry operations.

The probability density functions (PDFs) of the relative errors for each snapshot ω_i in the test datasets at $Re = \{40, 100, 400\}$,

$$\varepsilon_i = \frac{\|\omega_i - \mathcal{A}(\omega_i)\|}{\|\omega_i\|}, \tag{C1}$$

is reported in figure 7. Each ω_i in the test datasets is symmetry-augmented by random continuous and discrete symmetry operations. As expected, the reconstruction accuracy decreases with Re as the spatio-temporal complexity of the flow increases. Longer tails are also clear as Re increases, likely reflecting the increasing proportion of high-dissipation bursting events in the test datasets.

-
- [1] T. A. Zaki, Turbulence from an observer perspective, *Annu. Rev. Fluid Mech.* **57**, 311 (2025).
- [2] K. Taira, S. L. Brunton, S. T. Dawson, C. W. Rowley, T. Colonius, B. J. McKeon, O. T. Schmidt, S. Gordeyev, V. Theofilis, and L. S. Ukeiley, Modal analysis of fluid flows: An overview, *AIAA journal* **55**, 4013 (2017).
- [3] S. L. Brunton, B. R. Noack, and P. Koumoutsakos, Machine learning for fluid mechanics, *Annu. Rev. Fluid Mech.* **52**, 477 (2020).
- [4] K. Fukami and K. Taira, Grasping extreme aerodynamics on a low-dimensional manifold, *Nature Communications* **14**, 6480 (2023).
- [5] K. Zeng, C. E. P. De Jesús, A. J. Fox, and M. D. Graham, Autoencoders for discovering manifold dimension and coordinates in data from complex dynamical systems, *Machine Learning: Science and Technology* **5**, 025053 (2024).
- [6] A. Cleary and J. Page, Characterizing the Reynolds number dependence of the chaotic attractor in two-dimensional turbulence with dimension-minimizing autoencoders, *Phys. Rev. E* **112**, 055105 (2025).
- [7] K. Fukami, K. Fukagata, and K. Taira, Super-resolution reconstruction of turbulent flows with machine learning, *J. Fluid Mech.* **870**, 106–120 (2019).
- [8] J. P. Williams, O. Zahn, and J. N. Kutz, Sensing with shallow recurrent decoder networks (2024), arXiv:2301.12011 [math.DS].
- [9] Y. Du, M. Wang, and T. A. Zaki, State estimation in minimal turbulent channel flow: A comparative study of 4DVar and PINN, *International Journal of Heat and Fluid Flow* **99**, 109073 (2023).
- [10] J. Page, Super-resolution of turbulence with dynamics in the loss, *J. Fluid Mech.* **1002**, R3 (2025).
- [11] M. Weyrauch, M. Linkmann, and J. Page, State estimation in homogeneous isotropic turbulence using super-resolution with a 4DVar training algorithm (2025), arXiv:2510.16904 [physics.flu-dyn].
- [12] E. Özalp, A. Nóvoa, and L. Magri, Real-time forecasting of chaotic dynamics from sparse data and autoencoders, *Computer Methods in Applied Mechanics and Engineering* **450**, 118600 (2026).
- [13] P. Clark Di Leoni, L. Lu, C. Meneveau, G. E. Karniadakis, and T. A. Zaki, Neural operator prediction of linear instability waves in high-speed boundary layers, *J. Comput. Phys.* **474**, 111793 (2023).
- [14] G. J. Chandler and R. R. Kerswell, Invariant recurrent solutions embedded in a turbulent two-dimensional Kolmogorov flow, *J. Fluid Mech.* **722**, 554–595 (2013).
- [15] A. Cleary and J. Page, Dynamical relevance of periodic orbits under increasing Reynolds number and connections to inviscid dynamics, *J. Fluid Mech.* **1020**, A52 (2025).
- [16] D. Kochkov, J. A. Smith, A. Alieva, Q. Wang, M. P. Brenner, and S. Hoyer, Machine learning-accelerated computational fluid dynamics, *Proc. Natl. Acad. Sci.* **118** (2021).
- [17] G. Dresdner, D. Kochkov, P. Norgaard, L. Zepeda-Núñez, J. A. Smith, M. P. Brenner, and S. Hoyer, Learning to correct spectral methods for simulating turbulent flows (2022).
- [18] M. Wang, Q. Wang, and T. A. Zaki, Discrete adjoint of fractional-step incompressible Navier-Stokes solver in curvilinear coordinates and application to data assimilation, *J. Comput. Phys.* **396**, 427 (2019).
- [19] X. Fan, X. Liu, M. Wang, and J.-X. Wang, Diff-FlowFSI: A GPU-optimized differentiable CFD platform for high-fidelity turbulence and FSI simulations (2025), arXiv:2505.23940 [physics.flu-dyn].
- [20] D. P. Kingma and J. Ba, Adam: A method for stochastic optimization (2017), arXiv:1412.6980 [cs.LG].
- [21] L. Jing, J. Zbontar, and Y. LeCun, Implicit rank-minimizing autoencoder, in *Advances in Neural Information Processing Systems*, Vol. 33, edited by H. Larochelle, M. Ranzato, R. Hadsell, M. Balcan, and H. Lin (Curran Associates, Inc., 2020) pp. 14736–14746.
- [22] M. Wang and T. A. Zaki, State estimation in turbulent channel flow from limited observations, *J. Fluid Mech.* **917**, A9 (2021).
- [23] Q. Wang, M. Wang, and T. A. Zaki, What is observable from wall data in turbulent channel flow?, *J. Fluid Mech.* **941**, A48 (2022).
- [24] G. Huang, Z. Liu, and K. Q. Weinberger, Densely connected convolutional networks, 2017 IEEE Conference on Computer Vision and Pattern Recognition (CVPR) , 2261 (2016).
- [25] D. Hendrycks and K. Gimpel, Gaussian error linear units (gelus) (2023), arXiv:1606.08415 [cs.LG].
- [26] S. Ioffe and C. Szegedy, Batch normalization: Accelerating deep network training by reducing internal covariate shift, in *Proceedings of the 32nd International Conference on Machine Learning*, Proceedings of Machine Learning Research, Vol. 37, edited by F. Bach and D. Blei (PMLR, Lille, France, 2015) pp. 448–456.
- [27] I. Loshchilov and F. Hutter, Decoupled weight decay regularization, in *International Conference on Learning Representations* (2019).